RSC Advances

PAPER

View Article Online
View Journal | View Issue

Cite this: *RSC Adv.*, 2023, **13**, 1684

Novel targeted pH-responsive drug delivery systems based on PEGMA-modified bimetallic Prussian blue analogs for breast cancer chemotherapy†

Qiang Chen,‡[a] Xiaoyu Huang,‡[b] Geyi Zhang,[c] Jiangnan Li,[a] Yang Liu[a] and Xu Yan*[a]

The development of novel nanoparticle-based drug delivery systems (nano-DDSs) with high loading capacity, low toxicity, precise targeting, and excellent biocompatibility remains urgent and important for the treatment of breast cancer (BC). Herein, novel BC-targeted nano-DDSs based on bimetallic Prussian blue analogs (PBA-DDSs) for intracellular doxorubicin (DOX) delivery and pH-responsive release were developed. Two kinds of bimetallic PBA, namely CuFe (copper–iron) PBA and CoFe (cobalt–iron) PBA, were synthesized by a coprecipitation method, followed by modification with polyethyleneglycol methacrylate (PEGMA) *via* surface-initiated atom transfer radical polymerization and immobilization with the AS1411 aptamer to obtain two kinds of novel BC-targeted nano-DDS. CuFePBA@PEGMA@AS1411 and CoFePBA@PEGMA@AS1411 showed high drug loading efficiency of 80% and 84%, respectively, for DOX, while 56.0% and 75.9% DOX release could be achieved under acidic pH conditions. *In vitro* cell viability and *in vivo* experiments proved the good biocompatibility of both PBA-DDSs. Cellular uptake and *in vivo* distribution suggested that both PBA-DDSs had efficient nucleolin-targeting capability, indicating the targeted delivery of DOX in tumor tissues. *In vivo* evaluation of anti-BC efficacy further confirmed that the obtained PBA-DDSs exhibited excellent therapeutic efficacy with limited side-effects. Therefore, the proposed novel PBA-DDSs can be used as secure and effective drug nano-DDSs for BC chemotherapy.

Received 20th October 2022
Accepted 23rd December 2022

DOI: 10.1039/d2ra06631a

rsc.li/rsc-advances

1. Introduction

Breast cancer (BC) is the most commonly diagnosed cancer among women and is also the leading cause of female mortality.[1] In Asia, the overall age-standardized BC incidence rates have rapidly increased to approximately 39 per 100 000 women; the major issue in BC epidemiology is the high proportion of women younger than 50 years old.[2] Traditional treatments for BC, including surgery, radiotherapy, chemotherapy, and hormone therapy, remain unsatisfactory, especially for high-grade, late-stage, or aggressive types of BC, which exhibit a high rate of metastasis, deteriorated relapse, or death.[3] Among these treatments, chemotherapy has played an essential role in the treatment of BC, whereas the lack of specificity induces low bioavailability of drug and multiple severe side-effects.[4] Nanoparticle (NP)-based drug delivery systems (nano-DDSs) with enhanced permeability and retention effect have become a promising therapeutic option for BC.[5] Several nanomedicine products, such as Doxil® (PEGylated liposomal/doxorubicin (DOX) hydrochloride) and Abraxane® (albumin-bound paclitaxel NP), have been extensively used for BC adjuvant therapy with favorable clinical outcomes.[6] Several nanomaterials have been commonly used as anti-BC drug carriers; these nanomaterials include polymeric dendrimers,[7] micelles,[8] quantum dots,[9] nanoemulsions,[10] gold NPs,[11] carbon nanotubes,[12] metal oxide NPs,[13] metal–organic frameworks (MOFs),[14,15] and covalent organic frameworks.[16] However, the development of novel nano-DDSs with high loading capacity, low toxicity, precise targeting, multifunction, excellent biocompatibility and stability is still urgent and important.[17]

MOFs, an emerging class of hybrid porous nanomaterials originating from metal ions or clusters bridged by organic

[a]*Department of Orthopedics, The First Affiliated Hospital of Zhengzhou University, No. 1, Jianshe East Road, Zhengzhou 450052, P. R. China. E-mail: yanxu27@163.com*
[b]*Department of Gastroenterology, The First Affiliated Hospital of Zhengzhou University, No. 1, Jianshe East Road, Zhengzhou 450052, P. R. China*
[c]*Department of Orthopedics, Yellow River Sanmenxia Affiliated Hospital of Henan University of Science and Technology, No. 2, Heping West Road, Sanmenxia 472000, P. R. China*

† Electronic supplementary information (ESI) available: Experimental section, basic characterizations of all samples, cellular uptake behaviors, MFI analysis, tumor inhibition rates and HE staining evaluation. See DOI: https://doi.org/10.1039/d2ra06631a

‡ These authors contributed equally to this work.

linkers, have drawn increasing attention in recent years.[18] MOFs exhibit remarkable advantages, such as controllable size, well-defined pore aperture and high porosities, tailorable composition and structure, versatile functionality, large surface areas, high loading capacity, improved biocompatibility and biodegradability, and have become promising candidates as nano-DDSs.[19] Prussian blue (PB), as a subclass of MOFs, is a typical hexacyanoferrate coordination compound approved by U.S. Food and Drug Administration for clinical radioactive exposure treatment due to its excellent biosafety in the human body.[20] However, the original NPs of PB (PBNPs) show low specific surface area with poor drug loading capability. Two approaches, including hollow mesoporous[21,22] and surface modifications,[23] are used to improve their surface area and drug loading capacity. Tian *et al.* developed a periodic mesoporous organosilica-coated PB with high surface area (866 $m^2\ g^{-1}$) and high drug loading power (260 μg mg^{-1}), showing effective inhibition against BC by inducing the apoptosis and necrosis of tumor cells.[24] Among PBs, PB analogs (PBAs) or PB-based derivatives as nano-DDSs with high drug loading capacity have been widely investigated;[25] PB-based nanocarriers with tumor-targeting and controllable release capabilities are rarely reported.[26] Outfield-responsive nano-DDSs can effectively control drug release in response to inherent (*e.g.*, pH, redox reagents, and enzymes) or external stimuli (*e.g.*, temperature, ionic strength, light irradiation, ultrasound, and magnetic field).[27] Hence, PB-based "smart" nanocarriers with high drug loading capacity, active tumor-targeting capability, and stimuli-responsive controllable release are promising candidates of nano-DDSs that can alleviate toxicity of anti-tumor drugs and reduce side effects on normal tissues. Cai *et al.* reported that Mn PBAs were facilely coated onto the outer surface and inner mesoporous channels of hollow mesoporous PBNPs to prepare HMPB-Mn, which released Mn^{2+} and DOX in a pH-triggering manner.[21] To make bimetallic MnFe-PBA/DOX which showed high pH-responsive drug release and efficiency in Michigan cancer foundation-7 (MCF-7) cells,[28] sodium citrate (SC) was used as a structure modifier and folic acid (FA) as a tumor target. However, bimetallic PBAs still show evident cytotoxicity at high doses, which restricts their bio-related application, especially *in vivo* anti-cancer therapy. Therefore, good biosafety, low cost, easy synthesis, and environment-friendly PBA alternatives are necessary for the treatment of BC.

The hydrophilic comb-like structure of poly(ethylene glycol) methacrylate (PEGMA) cross-section had been used to enhance the biocompatibility of nanocarriers.[29] Lale *et al.* developed an atom-transfer radical polymerization (ATRP)-based poly-PEGMA–poly(caprolactone)–polyPEGMA for targeted delivery of DOX to cancer cells.[30] Huang *et al.* applied ATRP to graft superparamagnetic iron oxide NPs (SPIONs) with poly(glycidyl methacrylate)-*co*-PEGMA, and FA was conjugated with SPION–P(GMA-*co*-PEGMA) *via* "click" chemistry to improve the targeting efficiency and biocompatibility of these NPs.[31] More importantly, PEGMA is sensitive to pH and commonly prepared by controlling polymerization *via* surface-initiated ATRP (SI-ATRP). This is one of the most effective ways to introduce polymer layers onto inorganic surface.[32,33] Among various stimuli, pH gradients have been extensively applied to design novel stimuli-responsive delivery systems for anticancer therapies, which are substantially critical due to the intracellular organelles and special acidic extracellular microenvironment of solid tumors.[34] Therefore, bimetallic PBAs are modified by PEGMA *via* surface initiated ATRP (SI-ATRP), they are hopeful to develop novel stimuli-responsive nano-DDSs for BC therapy.

In this study, we developed a BC-targeted nano-DDS based on PBA (PBA-DDS) for DOX intracellular delivery and pH-responsive release. Two kinds of bimetallic PBA (CuFe PBA and CoFe PBA) were modified with PEGMA *via* SI-ATRP (denoted as CuFePBA@PEGMA and CoFePBA@PEGMA, respectively), followed by immobilization with AS1411 to improve their BC-targeted delivery capability (denoted as CuFePBA@PEGMA@AS1411 and CoFePBA@PEGMA@AS1411). Subsequently, DOX was loaded onto these PBAs (denoted as CuFePBA@PEGMA@AS1411/DOX and CoFePBA@PEGMA@AS1411/DOX). Scheme 1 illustrates the synthesis procedure used in this study. 3-(4,5-Dimethylthiazol-2-yl)-2,5-diphenyltetrazolium bromide (MTT) assay was used to measure cell viability of various cell types, such as human BC cell (MCF-7), mouse BC cell (4T1), and normal mouse fibroblast (L929), to investigate the *in vitro* biocompatibility of the analogs. Tissue sections and *ex vivo* images of vital organs, including heart, liver, spleen, lung, and kidney, were obtained to detect the *in vivo* biocompatibility and biodistribution of the analogs. Cell imaging and cellular behavior study were performed by confocal laser scanning microscopy and transmission electron microscopy (TEM). *In vivo* imaging and tumor sections of 4T1 xenograft tumor model were used to further investigate the efficacy of anti-BC treatment. PBA-DDS exhibited high DOX loading efficiency, good biocompatibility, excellent pH-responsive ability, excellent pH-responsive capability, well-controlled release of DOX in BC cells and thus less DOX-induced side-effects.

2. Experimental section

The S1 section (see the ESI†) lists the parts of chemicals and materials, synthesis and cytotoxicity assays of CuFe PBA, CoFe PBA, CuFePBA@PEGMA and CoFePBA@PEGMA, and their basic characterizations.

2.1 Preparation of CuFe PBA-DDS and CoFe PBA-DDS

CuFePBA@PEGMA and CoFePBA@PEGMA powders (100 mg) were separately dispersed in 100 mL of Milli-Q water to produce a homogenous suspension (1 mg mL^{-1}). The aptamer AS1411 solution (1 mL, 1 μM) was added into CuFePBA@PEGMA or CoFePBA@PEGMA suspensions (4 mL, 1 mg mL^{-1}) below stirring in the darkness for one day at room temperature. The suspension was then dialyzed against DI water for two days at room temperature to clear physically adsorbed or unloaded AS1411 molecules away, the dialysate was replaced every 4 h during this process.

5 mg of CuFePBA@PEGMA@AS1411 and CoFePBA@PEGMA@AS1411 were separately added into the DOX solution

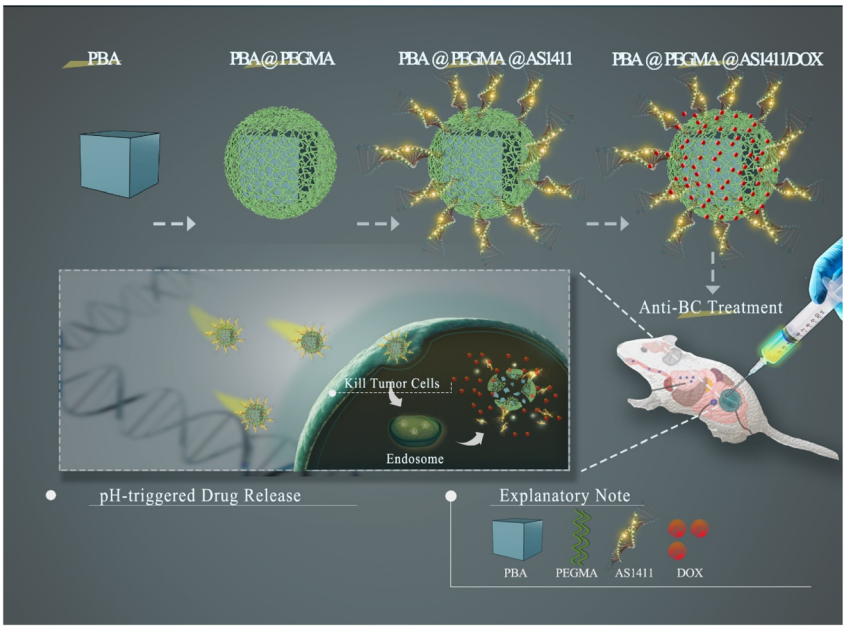

Scheme 1 Schematic illustration of the synthetic procedure for core–shell-structured PBA@PEGMA@AS1411-based DOX loading and pH-responsive controlled release system.

(5 mL, 1 mg mL^{-1}) and then stirred for one day in the darkness to achieve adequate adsorption. After, the solutions were washed with deionized water trice after centrifugation to remove physically adsorbed or unloaded DOX.

2.2 *In vitro* pH-responsive DOX release behavior

The CuFePBA@PEGMA@AS1411/DOX or CoFePBA@PEGMA@AS1411/DOX suspension (5.0 mL, 1 mg mL^{-1}) was put into the dialysis bag (MWCO 3500 Da) against 1× PBS (100 mL) with pH at 5.0 or 7.4. The dialysis bags were placed in the thermostatic shaker with 180 rpm at 37 °C. 3 mL dialysate was then collected at the desired intervals (0.5, 2, 4, 6, 8, 10, 12, 14, 25, 30, 36, 54, 80, 108, and 120 h), followed by adding 3 mL of fresh 1× PBS.

2.3 *In vitro* anti-BC efficacy assessment

As for *in vitro* anti-BC efficacy, the MTT assay (see the S1.5 for details†) was performed to detect the cell viability. 1×10^4 cells were typically seeded onto each well of the 96 well-plates overnight. Then, the cells were dealt with distinct densities (5, 10, 20, 40, 80, and 160 μg mL^{-1}) of DOX, CuFePBA@PEGMA@AS1411, CuFePBA@PEGMA@AS1411/DOX, CoFePBA@PEGMA@AS1411 and CoFePBA@PEGMA@AS1411/DOX for 12 hours, respectively. Afterward, the cells were cleaned and further cultured with DMEM for another 12 h. Then, 20 μL MTT solution (5.0 mg mL^{-1}) was then added to per well and cultured for 4 h. Finally, the medium was removed and dimethyl sulfoxide (150 μL) was added into each well. After sufficient shaking, the absorbance of each well was observed at 490 and 630 nm using a microplate reader, and the anti-BC efficacy was calculated accordingly.

2.4 *In vitro* imaging and intracellular distribution

As for *in vitro* imaging, cellular uptake of CuFePBA@PEGMA@AS1411/DOX and CoFePBA@PEGMA@AS1411/DOX were observed in MCF-7, 4T1, and L929 cells *via* CLSM (LSM710, ZEISS, Germany). Briefly, cells were seeded in the glass-bottom dish (1×10^5 cells) and cultured at 5% CO_2 and 37 °C overnight. Then, CuFePBA@PEGMA@AS1411/DOX and CoFePBA@PEGMA@AS1411/DOX (20 μL, 5 mg mL^{-1}) were added and cultured for 2 hours. After washing with PBS thrice, the cells were fixed with paraformaldehyde (4%) at 37 °C for 10 min in dark. Subsequently, the cells were rinsed and incubated with Hoechst 33342 (nucleus-staining, 300 nM) at 37 °C for 15 min. After washing three times, the cells were observed by the CLSM with a 20× objective lens (E_x/E_m of Hoechst 33342: 405/450–480 nm; E_x/E_m of Cy3-AS1411: 515/550–570 nm; E_x/E_m of DOX 488/580–620 nm).

To observe the cellular distribution of CuFePBA@PEGMA@AS1411, CuFePBA@PEGMA@AS1411/DOX, CoFePBA@PEGMA@AS1411 and CoFePBA@PEGMA@AS1411/DOX, the transmission electron microscopy (TEM) was applied. 4T1 cells (1×10^5 cells each well) were seeded in 6-well plates and incubated for one day, then 20 μL of CuFePBA@PEGMA@AS1411, CuFePBA@PEGMA@AS1411/DOX, CoFePBA@PEGMA@AS1411 or CoFePBA@PEGMA@AS1411/DOX (1 mg mL^{-1}) was added into each well and incubated for 30 min. After washing by cold PBS thrice, the fresh cell samples were obtained by trypsin digestion and centrifugation. Subsequently, the samples were first fixed with 2% glutaraldehyde solution overnight at 4 °C and followed by the secondary fixation with 1% osmium tetroxide for 2 hours. The samples were dehydrated in a graded series of ethanol and finally with propylene oxide. Then, the samples were implanted in Epon

resin. 70 nm or so slight sections were made ready with the PowerTome-XL ultramicrotome (RMC, USA). Finally, the JEM-2100F high-resolution transmission electron microscope (HR-TEM, JEOL, Japan) were used to observe the sections with a voltage of 120 kV.

2.5 *In vivo* biodistribution

Healthy female BALB/c mice of 14–16 g body weight were procured from the Experimental Animal Center of Zhengzhou University with free access to food and water in standard animal equipment and authorized by Zhengzhou University's Animal Ethics Committee. After one-week adaptive feeding, mice were injected with CuFePBA@PEGMA@AS1411/DOX and CoFePBA@PEGMA@AS1411/DOX (10.0 mg kg^{-1}) through tail vein. Afterward, mice were sacrificed at various time-points (0, 1, 4, and 24 h post-injection), and the crucial organs (heart, lung, spleen, liver, and kidney) were collected to perform *in vitro* imaging by adopting the IVIS Lumina III system (PerkinElmer) with an appropriate E_x/E_m of 480/590 nm.

2.6 *In vivo* imaging

BALB/c nude mice (female, 18 g body weight) were acquired from Hunan Slaccas Jingda Laboratory Animal Co., Ltd (Hunan, China) and housed in the specific pathogen free (SPF) animal facility with free access to food and water. After one-week adaptive feeding, 4T1 cells suspended in PBS (1×10^6 cells per 100 μL per mouse) were subcutaneously injected into the right axillary region. To calculate the volume (V) of tumor, the width (W) and length (L) was measured by electronic vernier caliper. Then, the volume of tumor was estimated according to the formula $V = (W^2 \times L)/2$. When the tumor volumes reached approximately 100 mm^3, the 4T1 tumor-bearing nude mice were randomly divided into 4 groups ($n = 4$), and were separately injected with 100 μL 0.9% saline, 100 μL DOX (0.5 mg mL^{-1}), 100 μL CuFePBA@PEGMA@AS1411/DOX (0.5 mg mL^{-1}) and 100 μL CoFePBA@PEGMA@AS1411/DOX (0.5 mg mL^{-1}). After treating for 30 min, the mice were imaged at IVIS Lumina III system (PerkinElmer) with an appropriate excitation/emission wavelength of 480/590 nm.

2.7 *In vivo* anti-BC assessment

Firstly, the animal model of BC was established by subcutaneously injecting 4T1 cells into the right axillary region of healthy female BALB/c mice (procured from Zhengzhou University's Lab Animal Center). The 4T1 tumor-bearing mice were separated to five groups (three mice for each group) when the tumor volumes achieved about 150–200 mm^3 randomly, and administered with 200 μL 0.9% saline, 200 μL DOX (0.5 mg mL^{-1}), 200 μL CuFePBA@PEGMA@AS1411/DOX (0.25, 0.5, and 1.0 mg mL^{-1}) *via* tail vein injection every two days. The body weight and tumor volume were noted every two days until 14 days post-injection. After a survival period of 14 days, the 4T1 xenograft-bearing mice were anesthetized by injecting 10% chloral hydrate (0.1 mL g^{-1}) into abdominal cavity. The tumors and vital organs including hearts, livers, spleens, lungs and kidneys were excised, harvested, fixed in 4% paraformaldehyde for 24 h, dehydrated, embedded in paraffin, sliced at 4 μm for hematoxylin and eosin (H&E) staining, and examined by using CLSM. The similar procedures were performed for CoFePBA@PEGMA@AS1411/DOX. The tumor inhibition rate (TIR) was accessed as TIR (%) = $(V_{control} - V_{drug})/V_{control} \times 100\%$, where $V_{control}$ and V_{drug} represented the tumor volumes in control and drug treated groups for 14 days, respectively.

2.8 Live subjects

The animal experiments have obtained the approvals from the Animal Care and Ethics Committee (ACEC) of Zhengzhou University in China. All animal experiments were performed in accordance with the statutory requirements of People's Republic of China (GB14925-2010).

3. Results

3.1 Crystal and chemical structures of CoFe PBA, CuFe PBA, CoFePBA@PEGMA, and CuFePBA@PEGMA

The chemical and crystal structures of CoFe PBA, CuFe PBA, CoFePBA@PEGMA, and CuFePBA@PEGMA were analyzed; their detailed description and discussion are shown in Section S2 (ESI).† The results verified that the crystallinity of PBA nanocubes decreased due to the coverage by the PEGMA layer, in which the chemical structures of PEGMA were determined by the Fourier transform infrared spectrum analysis of CoFePBA@PEGMA and CuFePBA@PEGMA. Moreover, variations in the chemical components and environments of CoFe PBA and CuFe PBA before and after modification by PEGMA were characterized by X-ray photoelectron spectroscopy (XPS). Fig. S2† shows the XPS survey spectra of all samples. The detailed expansions are supplied in Section S2.1 (ESI).† In addition, changes in the chemical environments and valence states of each element containing in CoFe PBA and CoFePBA@PEGMA were probed by their high-resolution XPS spectra. The high-resolution Co 2p, Fe 2p, C 1s, and N 1s XPS spectra of CoFe PBA and CoFePBA@PEGMA were deconvoluted and analyzed by the XPSPEAK41 software (Fig. S3†). As shown in Fig. S3a1,† the Co 2p XPS spectrum of CoFe PBA was separated into two spin–orbit doublets at the binding energies (BEs) of 782 (Co $2p_{3/2}$) and 797.24 eV (Co $2p_{1/2}$) with a difference of 15.2 eV. The average BEs of Co $2p_{3/2}$ were recorded at 781.5 and 782.6 eV for Co^{2+} and Co^{3+}, respectively.[35] The peaks at 784.1 and 787.7 eV were associated with the shake-up satellite of Co $2p_{3/2}$.[36] These findings suggest the mixed chemical valences of Co^{2+} and Co^{3+} in CoFe PBA. As for Fe 2p XPS spectrum, the peaks at the BEs of 710.2 and 723.5 eV were assigned to Fe^{3+} $2p_{3/2}$ and Fe^{3+} $2p_{1/2}$, respectively. The peaks at 715.2, 719.0, and 735.6 eV were satellite peaks of Fe $2p_{3/2}$ and Fe $2p_{1/2}$. Above results indicate that Fe and Co existed in CoFe PBA nanocubes as mixed valances. However, the signals of Co 2p and Fe 2p remarkably decreased in CoFePBA@PEGMA (Fig. S3a2 and b2†). The CoFe PBA nanocubes were totally covered by the PEGMA layer. As such, the chemical components of CoFe PBA cannot be determined by XPS because of the limitation of its

test thickness.[37] As for the high-resolution C 1s XPS spectrum of CoFe PBA and CoFePBA@PEGMA (Fig. S3c1 and c2,† respectively), four peaks at 284.5 (C–C), 285.0 (C–N), 285.6 (C–O), and 288.3 (N–C=O) eV were fitted out. As displayed in Fig. S3d1 and d2,† the peaks at the BEs of 399.7 and 397.5 eV were ascribed to N–C=O and C≡N, respectively.[38] After the modification of PEGMA, the peak area of C–O increased, and that of C≡N decreased, consistent with the external structure of CoFePBA@PEGMA.

The high-resolution XPS spectra for CuFe PBA and CuFePBA@PEGMA were also deconvoluted. As shown in Fig. S4a1 and a2,† the Cu 2p XPS spectrum of CuFe PBA exhibited two main peaks at the BEs of 935.3 and 955.6 eV, which were assigned to Cu $2p_{3/2}$ and Cu $2p_{1/2}$ of Cu^{2+}, respectively.[39] The BE of 932.6 eV was ascribed to Cu^{+},[40] and the BE of 935.2 eV was due to Cu(II) species.[41] After modification with PEGMA, a new peak of CuFePBA@PEGMA appeared at 933.7 eV (Fig. S4a2†), and it may be ascribed to the existence of low amount of CuO.[42] Moreover, two satellite peaks, namely, the "shake-up" peaks, were observed, indicating the existence of Cu^{2+}. As for the Fe 2p XPS spectra, two peaks at the BEs of 710 and 723 eV were fitted out in CuFe PBA, corresponding to Fe $2p_{3/2}$ and Fe $2p_{1/2}$, respectively.[43] The Fe $2p_{3/2}$ spectrum was deconvoluted into two peaks at the BEs of 708.2 and 709.8 eV, which were attributed to Fe^{2+} and Fe^{3+}, respectively. The Fe 2p signal (Fig. S4b2†) was weakened due to the PEGMA layer. Similar analysis results were observed in the N 1s XPS spectra of CuFe PBA and CuFePBA@PEGMA (Fig. S4c1 and c2,† respectively) and those of CoFe PBA and CoFePBA@PEGMA. Additionally, a strong Br 3d XPS signal was obtained with CoFePBA@PEGMA and CuFePBA@PEGMA (Fig. S5†), and this finding resulted from the anchoring of SI-ATRP initiator, that is, 2-bromoisobutyl bromide, which was applied to initiate monomer polymerization over the PBA surface.[44] Over all, the schemes of chemical structures and synthesis steps for CuFePBA@PEGMA@AS1411 and CoFePBA@PEGMA@AS1411 have shown in Fig. S6.†

3.2 Surface morphologies and nanostructures of CoFe PBA, CuFe PBA, CoFePBA@PEGMA, and CuFePBA@PEGMA

The surface morphologies and nanostructures of CoFe PBA and CoFePBA@PEGMA were characterized by field-emission scanning electron microscopy (SEM) and high-resolution TEM (HR-TEM) (Fig. 1). Fig. 1a shows that CoFe PBA demonstrated a nanocube shape form with the inhomogeneous size (80–120 nm) and coarse surface. The high-magnification SEM image of CoFe PBA (Fig. 1b) revealed that the CoFe PBA nanocube displayed a porous structure, which greatly boosted the adsorption of DOX.[45] The TEM image of CoFe PBA (Fig. 1c) confirmed the nanocube structure. No clear lattice spacing was observed in the HR-TEM image of CoFe PBA (Fig. 1e), suggesting its low crystallinity.

In terms of CoFePBA@PEGMA, the CoFe PBA nanocubes were inserted with a polymer layer, resulting in the loss of the nanocube shape (Fig. 1f and g). As shown in its TEM image (Fig. 1h), the CoFePBA@PEGMA composite was dispersed into small NPs with sizes of 5–20 nm (Fig. 1i). The HR-TEM image of

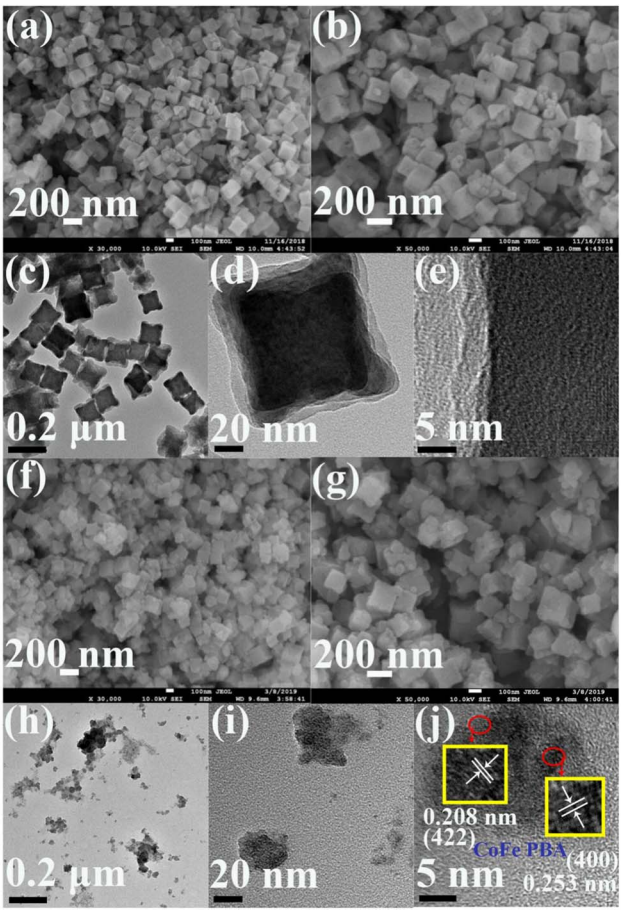

Fig. 1 (a and b) Low- and high-magnification SEM images and (c–e) TEM and HR-TEM images of CoFe PBA. (f and g) Low- and high-magnification SEM images and (h–j) TEM and HR-TEM images of CoFePBA@PEGMA composite.

the CoFePBA@PEGMA composite (Fig. 1j) showed three types of lattice fringes with spacings of 0.208, 0.228, and 0.253 nm, which were attributed to the (422), (420), and (400) planes of CoFe PBA, respectively.

A nanocube shape was also obtained for CuFe PBA, as observed from its SEM image (Fig. 2a). The nanocube size of CuFe PBA was uneven and ranged from 100–180 nm, as shown in the high-magnification SEM image (Fig. 2b). The TEM image of CuFe PBA (Fig. 2c) also indicated its inhomogeneous nanocube size, and the deep black color further revealed its solid structure (Fig. 2d). No clear lattice fringe was obtained in the HR-TEM of CuFe PBA (Fig. 2e), hinting its low crystallinity. After the modification with PEGMA, the nanocubic particles were accumulated by PEGMA, as indicated in the SEM image of CuFePBA@PEGMA (Fig. 2f and g). The similarly small NPs of CuFePBA@PEGMA were observed in the TEM image (Fig. 2h), also suggesting its excellent dispersion capability in aqueous solutions (Fig. 2i). In the HR-TEM image of CuFePBA@PEGMA (Fig. 2j), clear lattices spacing of 0.251, 0.223, 0.204, and 0.302 nm were contributed by the (400), (420), (422), and (311) planes of $Cu_2Fe(CN)_6$ nanocube, respectively.[46]

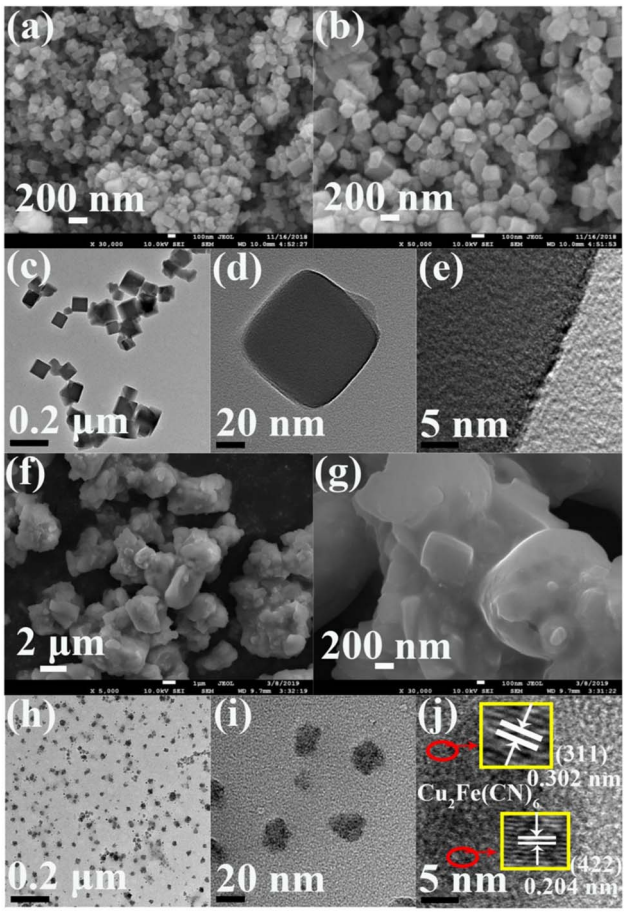

Fig. 2 (a and b) Low- and high-magnification SEM images and (c–e) TEM and HR-TEM images of CuFe PBA. (f and g) Low- and high-magnification SEM images and (h–j) TEM and HR-TEM images of CuFePBA@PEGMA composite.

3.3 DOX loading and *in vitro* pH-responsive drug release

Herein, DOX was selected as a model drug to explore the drug loading and release of PBA-based nano-DDSs. The DOX-loading efficiency was 33% for both CuFe PBA and CoFe PBA, whereas CuFePBA@PEGMA and CoFePBA@PEGMA exhibited remarkably high DOX-loading efficiencies of 80% and 84%, respectively, after the modification with PEGMA. The results confirmed that the high drug loading capacities of CuFePBA@PEGMA and CoFePBA@PEGMA were attributed to the strong hydrophobic interaction between PEGMA and DOX.[47] To further investigate the stimuli-responsive drug release behavior of PBA-DDS, we dispersed CuFePBA@PEGMA/DOX, CuFePBA@PEGMA@AS1411/DOX, CoFePBA@PEGMA/DOX, and CoFePBA@PEGMA@AS1411/DOX in 1× phosphate buffered saline (PBS) with different pH. As shown in Fig. 3A and C, CuFe PBA and CoFe PBA barely showed pH-dependent DOX release behavior. However, PEGMA-modified CuFe PBA and CoFe PBA exhibited pH-dependent DOX release behavior. As for CuFePBA@PEGMA@AS1411, the DOX maximum release was achieved at 48 h, with 56% and 23% released at pH 5.0 and 7.4, separately (Fig. 3B). Similar behaviors can be observed for CoFePBA@PEGMA@AS1411 (Fig. 3D). DOX release increased to 75% at pH 5.0. Moreover, the pH-responsive DOX release profiles of CuFePBA@PEGMA and CoFePBA@PEGMA were investigated in PBS solutions at pH of 5.0 and 7.4. A total of 58.2% and 65.8% DOX releases were observed in the original 24 h at pH = 5.0 and leveled off at 48 h with values of 68% and 75%, respectively (Fig. S7†). Thus, PEGMA modification endowed the nano-DDSs with pH-triggered drug-release behaviors due to the increased solubility and surface modification with PEGMA,[48,49] and the modification of targeted aptamer AS1411 showed no influence on the pH-controlled releasing property. Therefore, the pH-responsive PBA-DDSs were favorable for improving the antitumor therapeutic effects.

3.4 *In vitro* biocompatibility and *in vitro* anti-BC efficacy

The cell viabilities of the four samples, including CuFe PBA, CuFePBA@PEGMA, CoFe PBA, and CoFePBA@PEGMA, were evaluated by MTT assay to determine their *in vitro* biocompatibility. The samples of CuFe PBA and CuFePBA@PEGMA exhibited fair cell viability (*ca.* 70%) toward MCF-7, 4T1, and L929 cells when the concentration was 80 μg mL^{-1} (Fig. 4A–C), which suggest the good biocompatibility of the designed nano-DDSs. CoFe PBA and CoFePBA@PEGMA exhibited high cell viability (*ca.* 80%) of MCF-7, 4T1, and L929 cells (Fig. 4D–F, respectively) when the concentration was 160 μg mL^{-1}.

Subsequently, the *in vitro* anti-BC efficacies of DOX, CuFePBA@PEGMA@AS1411, CuFePBA@PEGMA@AS1411/DOX, CoFePBA@PEGMA@AS1411, and CoFePBA@PEGMA@AS1411/DOX were measured by MTT assay. As shown in Fig. 4G and J, the cell viability of MCF-7 cells treated with DOX, CuFePBA@PEGMA@AS1411/DOX, and CoFePBA@PEGMA@AS1411/DOX significantly decreased to 44.2%, 45.3%, and 48.0% when the concentration was 20 μg mL^{-1}, respectively. Thus, CuFePBA@PEGMA@AS1411/DOX and CoFePBA@PEGMA@AS1411/DOX showed equivalent cytotoxicity as free DOX when the low concentration was 20 μg mL^{-1}. As the concentrations increased, the cell viability further reduced, suggesting a significant anti-tumor efficacy. Similar results can be observed in mouse 4T1 cells (Fig. 4H and K). The cytotoxicity of DOX, CuFePBA@PEGMA@AS1411/DOX, and CoFePBA@PEGMA@AS1411/DOX against normal L929 cells showed remarkably different behaviors (Fig. 4I and L). Free DOX exhibited significant toxicity to L929 cells at the low density of 5 μg mL^{-1}, CuFePBA@PEGMA@AS1411/DOX and CoFePBA@PEGMA@AS1411/DOX presented mild toxicity, and above 60% of L929 cells were alive at the dose of 10 μg mL^{-1}. The cell viability of normal L929 cells was still *ca.* 70–80% at the highest concentration of CuFePBA@PEGMA or CoFePBA@PEGMA (160 μg mL^{-1}), further indicating their good *in vitro* biocompatibility. In our previous study, about 30–60% of L929 cells were alive when dealt with a series of MnFe PBAs at high dosage (80 μg mL^{-1}), and the MnFe PBA drug nanocarriers demonstrated greater cytotoxicity to normal L929 cells than to tumor MCF-7 cells.[28] These results indicate that the novel PBA-DDS nano-carrier exhibited improved *in vitro* biocompatibility and good anti-BC efficacy.

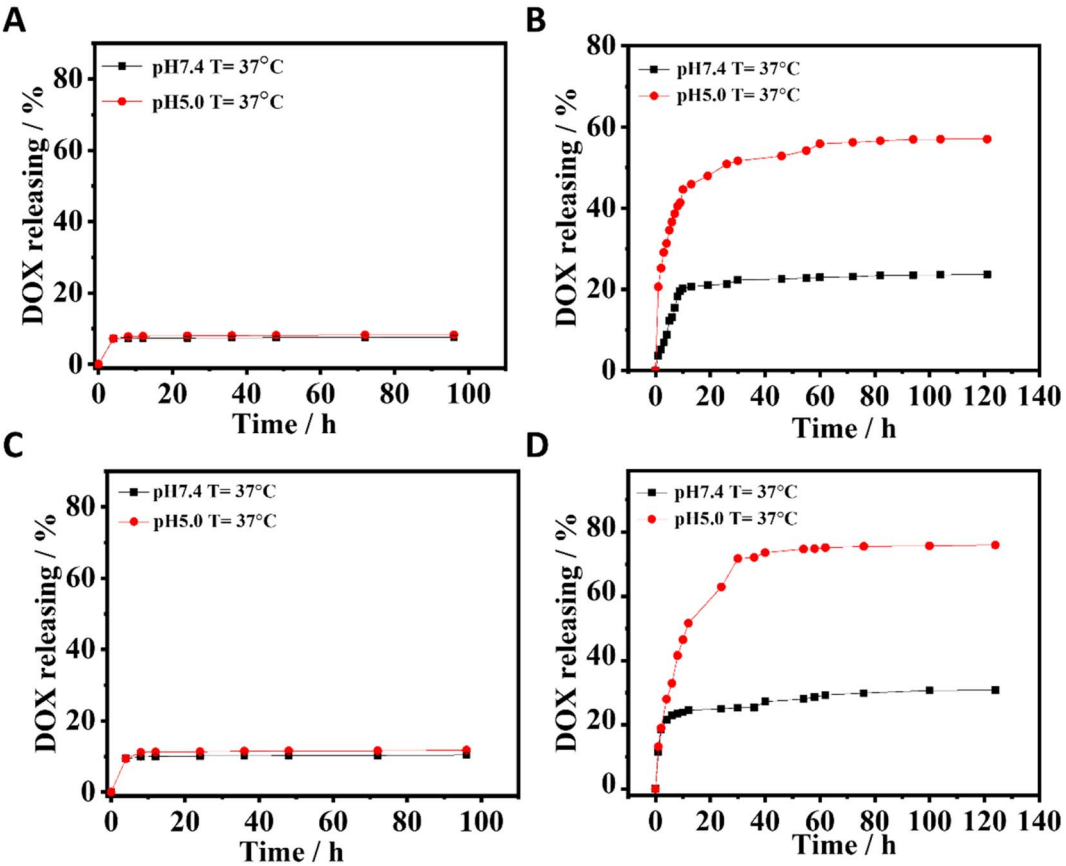

Fig. 3 The pH-dependent DOX release of (A) CuFePBA/DOX, (B) CuFePBA@PEGMA@AS1411/DOX, (C) CoFePBA/DOX, and (D) CoFePBA@PEGMA@AS1411/DOX.

3.5 Cellular uptake and intracellular distribution

AS1411 is a synthetic 26-nucleotide phosphodiester oligodeoxynucleotide (*i.e.*, unmodified DNA) with the sequence, 5′-GGTGGTGGTGGTTGTGGTGGTGGTGG, and specifically binds to nucleolin, which is highly expressed on the surface of BC cell membrane.[50–52] To investigate the cellular behavior, Cy3-AS1411 with yellow fluorescence was adopted. As shown in Fig. S8,† the yellow fluorescence intensity in MCF-7 and 4T1 cells treated by CuFePBA@PEGMA@AS1411/DOX and CoFePBA@PEGMA@AS1411/DOX was stronger than that in L929 cells, which indicates that CuFePBA@PEGMA@AS1411/DOX and CoFePBA@PEGMA@AS1411/DOX were internalized by BC cells (MCF-7 and 4T1) *via* AS1411-mediated cell uptake. The nano-DDSs were mainly distributed in the cytoplasm. To further confirm the AS1411 specifically mediated endocytosis, we analyzed the mean fluorescence intensity (MFI) of the entire cell by selecting three different visual fields containing 10–20 cells in three parallel experiments. The MFI of the entire cell was analyzed in all nine images by using ImageJ software. The results showed that the MFI of AS1411 in MCF-7 cells was significantly higher than that in L929 cells ($P < 0.05$), and no significant difference was observed between MFI of AS1411 in 4T1 cells and that in L929 cells (Fig. S9†). Liao *et al.* reported that AS1411-functionalized NPs remarkably promoted the affinity and binding to nucleolin receptors, enhancing the subsequent intracellular uptake and trafficking.[53] The underlying mechanism of internalization of AS1411-functionalized NPs can be related to micropinocytosis in a nucleolin expression-dependent manner.[54] Furthermore, the cellular uptake behaviors of CuFePBA@PEGMA@AS1411/DOX and CoFePBA@PEGMA@AS1411/DOX were investigated at pH = 6.0 to simulate the tumor acid microenvironment (Fig. 5). The MFI analysis of DOX exhibited that the MFI of nano-DDS in MCF-7 and 4T1 cells was significantly higher than that in L929 cells ($P < 0.05$). Thus, more DOX can be released in MCF-7 and 4T1 cells (Fig. S10†).

For further investigation of the intracellular distribution of the designed nano-DDSs, the cryo-TEM technique was used to observe the cellular ultrastructure. CuFePBA@PEGMA@AS1411, CuFePBA@PEGMA@AS1411/DOX, CoFePBA@PEGMA@AS1411, and CoFePBA@PEGMA@AS1411/DOX were mainly distributed within the endosomes and lysosomes, further confirming the AS1411-mediated cellular endocytosis (Fig. 6). Moreover, endocytic structural collapse was observed in the 4T1 cells treated by CuFePBA@PEGMA@AS1411/DOX and CoFePBA@PEGMA@AS1411/DOX, hinting the intracellular drug release and anti-tumor effect. The difficulty of controlling drug release at an intracellular level continues to be a key challenge for improving the efficacy and safety of anti-tumor

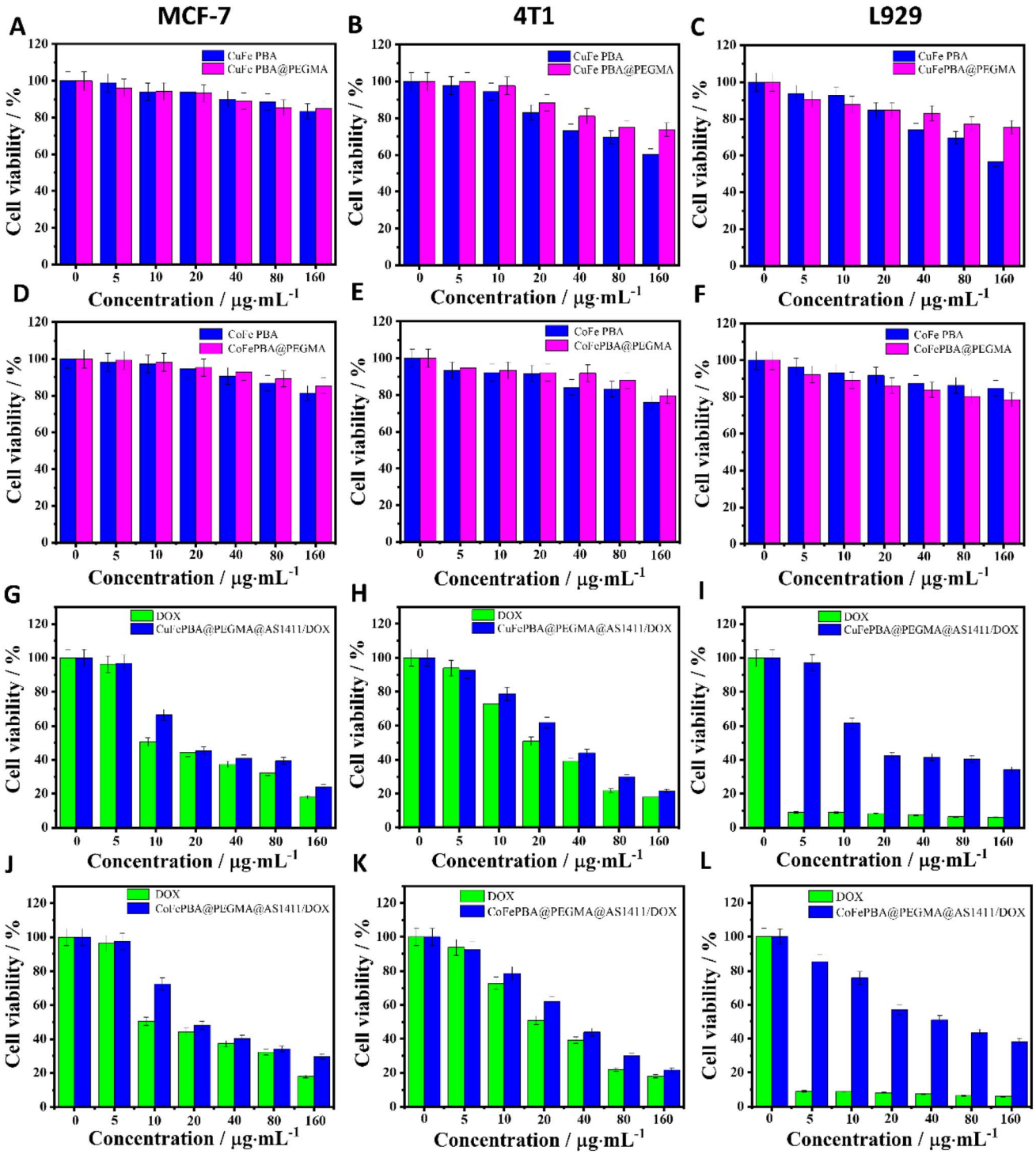

Fig. 4 Cytotoxicity assays. *In vitro* biocompatibility of CuFe PBA and CuFePBA@PEGMA in MCF-7 (A), 4T1 (B) and L929 cells (C); *in vitro* biocompatibility of CoFe PBA and CoFePBA@PEGMA in MCF-7 (D), 4T1 (E) and L929 cells (F); *in vitro* anti-BC efficacy of DOX and CuFePBA@PEGMA@AS1411/DOX in MCF-7 (G), 4T1 (H) and L929 cells (I); *in vitro* anti-BC efficacy of DOX and CoFePBA@PEGMA@AS1411/DOX in MCF-7 (J), 4T1 (K) and L929 cells (L).

therapy.[55] The current results suggest that the designed CuFePBA@PEGMA@AS1411/DOX and CoFePBA@PEGMA@AS1411/DOX have great potential as controlled intracellular drug-release nano-carriers for BC nano-therapy.

3.6 *In vivo* biodistribution

To directly observe the *in vivo* biodistribution of CuFePBA@PEGMA@AS1411/DOX and CoFePBA@PEGMA@AS1411/DOX, healthy mice were used as

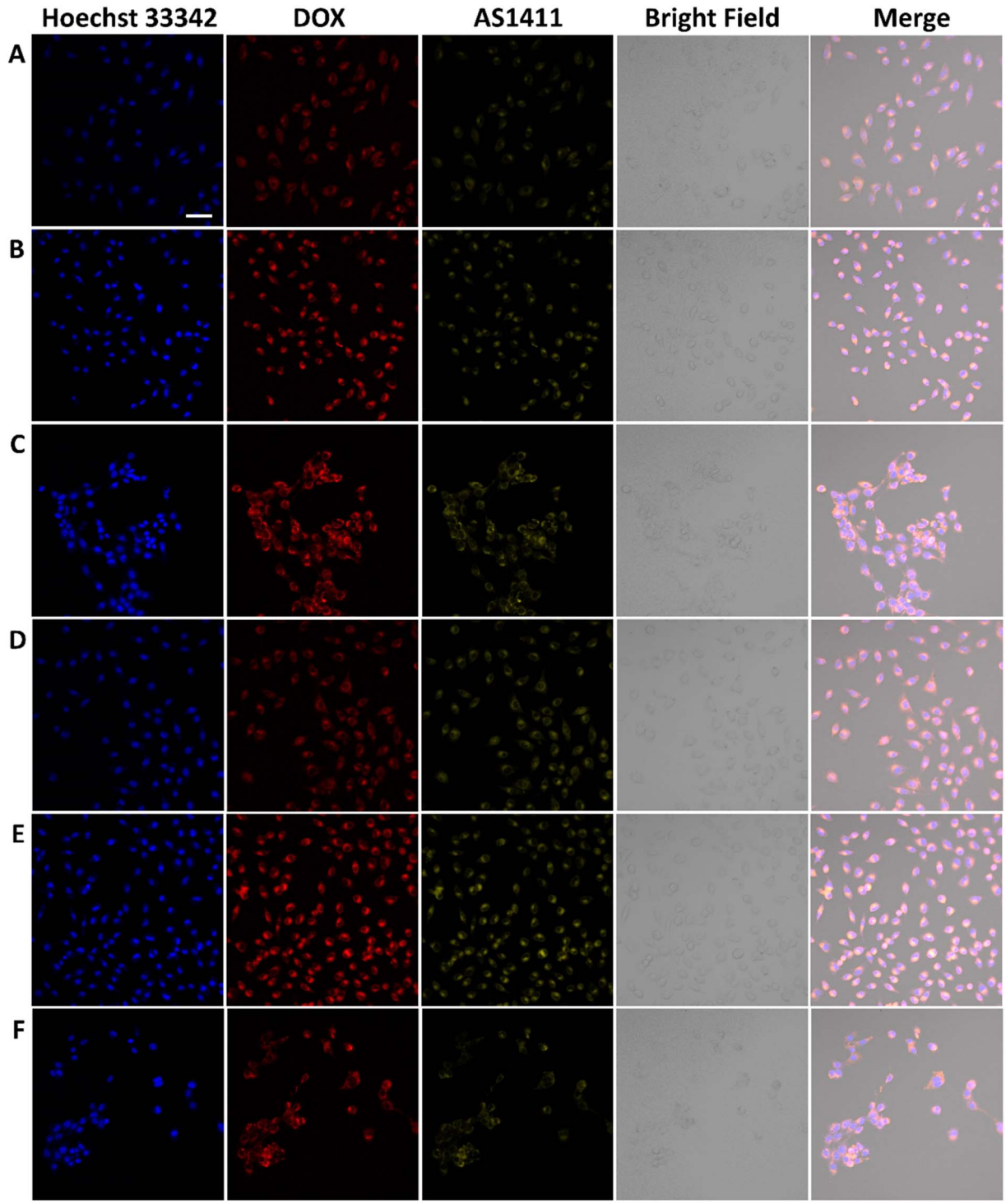

Fig. 5 Cellular uptake behaviors of CuFePBA@PEGMA@AS1411/DOX in L929 (A), MCF-7 (B), and 4T1 cells (C) and CoFePBA@PEGMA@AS1411/DOX in L929 (D), MCF-7 (E), and 4T1 cells (F) at pH = 6.0. (The scale bar is 40 μm.)

the model. The *in vivo* fluorescence images of crucial organs (heart, lung, spleen, liver, and kidney) were collected after intravenous injection for different durations (Fig. 7). As shown in Fig. 7A–E, CuFePBA@PEGMA@AS1411 was mostly distributed in the kidney and liver 1 h post-injection. A small part of CuFePBA@PEGMA@AS1411 was distributed in the lung. At 4 h post-injection, CuFePBA@PEGMA@AS1411 only resided within kidney and liver. After 24 h, almost no fluorescence was observed, indicating that CuFePBA@PEGMA@AS1411 was metabolized within 24 h. The renal clearable NPs can accelerate body clearance of an off-target drug and reduce its side effects during anti-tumor therapy.[56] As shown in Fig. 7F–J,

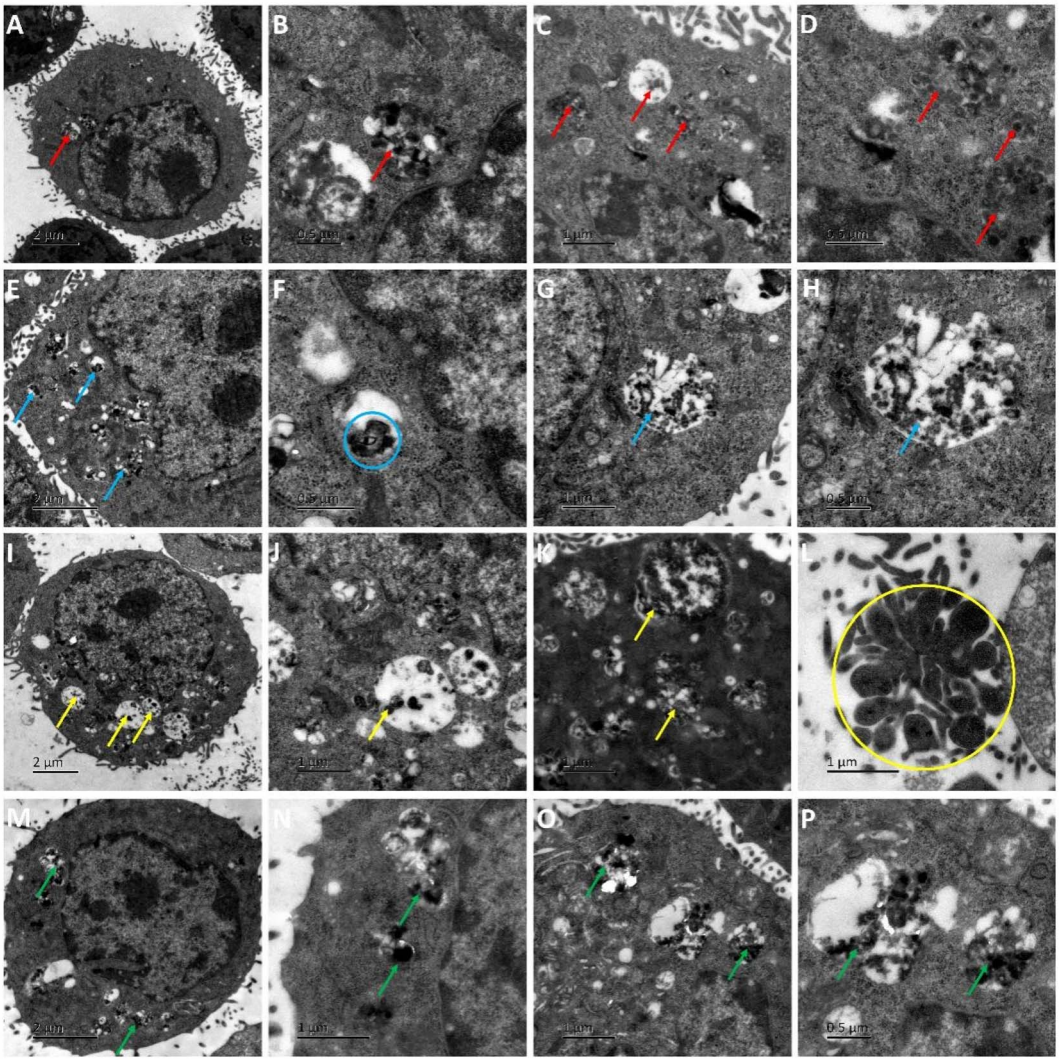

Fig. 6 Intracellular distribution of CuFePBA@PEGMA@AS1411 (A–D), CuFePBA@PEGMA@AS1411/DOX (E–H), CoFePBA@PEGMA@AS1411 (I–L) and CoFePBA@PEGMA@AS1411/DOX (M–P) in 4T1 cells. Arrows indicated that internalized CuFePBA@PEGMA@AS1411 (red arrows), CuFePBA@PEGMA@AS1411/DOX (blue arrows), CoFePBA@PEGMA@AS1411 (yellow arrows), CoFePBA@PEGMA@AS1411/DOX (green arrows) resided within endosomes and lysosomes. Blue circle indicated the structural changes of CuFePBA@PEGMA@AS1411/DOX and yellow circle indicated the apoptotic body.

CuFePBA@PEGMA@AS1411/DOX was mostly dispersed in the kidney, liver, and lung post-injection. A small part of CuFePBA@PEGMA@AS1411/DOX was distributed in the heart. After 24 h post-injection, the fluorescence signals decreased in the kidney, liver, and lung, which might indicate the possible metallization by the immune response of the mice. Compared with CuFePBA@PEGMA@AS1411/DOX, CoFePBA@PEGMA@AS1411/DOX showed a similar *in vivo* biodistribution. After 24 h, the CoFePBA@PEGMA@AS1411 was still distributed in the liver and kidney, indicating a low excretion rate (Fig. 7O).

3.7 *In vivo* anti-BC assessment

The *in vivo* anti-BC efficacy of CuFePBA@PEGMA@AS1411/DOX and CoFePBA@PEGMA@AS1411/DOX was assessed by using 4T1 tumor-bearing mice. As shown in Fig. 8A, 1.0 mg mL^{-1} CuFePBA@PEGMA@AS1411/DOX-treated mice showed the smallest tumor size compared with the control and other treatment groups. Furthermore, the tumor volumes of mice were monitored during the whole treatment periods (Fig. S11A and C†). The tumor volume of mice treated with 0.9% saline reached almost 1239.3 ± 61.9 mm^3 after 15 days, whereas that of mice treated with 0.5 mg mL^{-1} free DOX decreased to 638.0 ± 31.9 mm^3. The tumor volumes of mice treated with 0.5 and 1.0 mg mL^{-1} CuFePBA@PEGMA@AS1411/DOX and CoFePBA@PEGMA@AS1411/DOX were approximately 450 and 380 mm^3, respectively, which are lower than that of mice treated with 0.5 mg mL^{-1} free DOX ($P < 0.05$), indicating the improved anti-BC efficacy. Mice in the DOX-treated group showed a significant decrease in body weight, whereas mice in the 0.9%

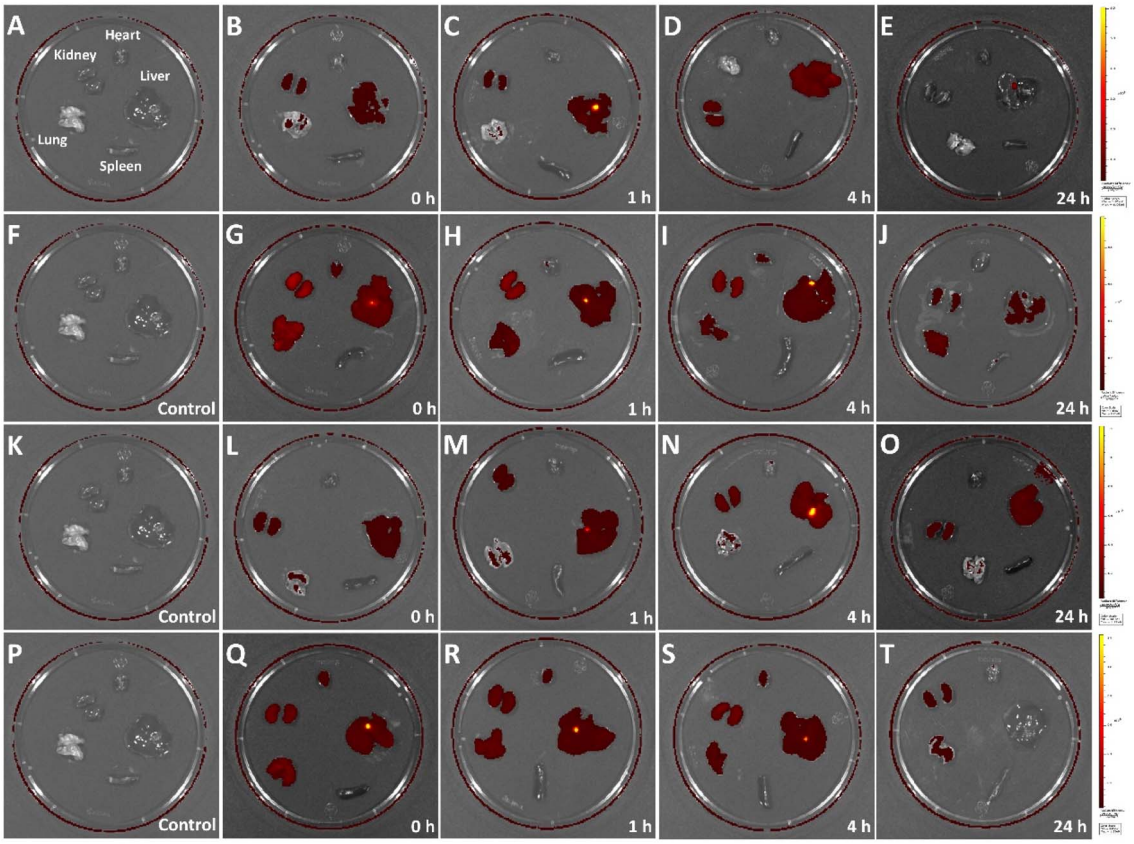

Fig. 7 *In vivo* biodistribution of CuFePBA@PEGMA@AS1411 (A–E), CuFePBA@PEGMA@AS1411/DOX (F–J), CoFePBA@PEGMA@AS1411 (K–O), and CoFePBA@PEGMA@AS1411/DOX (P–T).

saline and CuFePBA@PEGMA@AS1411/DOX-treated groups showed almost no decrease in body weight ($P < 0.05$) (Fig. S11B and D†). Similar results were observed in the CoFePBA@PEGMA@AS1411/DOX-treated groups (Fig. 8B). The tumor inhibition rates of CuFePBA@PEGMA@AS1411/DOX and CoFePBA@PEGMA@AS1411/DOX were calculated and reached approximately 70.1% and 70.5% of the concentration of 1.0 mg mL^{-1}, respectively, which were remarkably higher than that of free DOX ($P < 0.05$, Fig. S12†). Thus, CuFePBA@PEGMA@AS1411/DOX and CoFePBA@PEGMA@AS1411/DOX exhibited excellent anti-BC efficacy and limited side effects. The tumor accumulation effects were investigated by *in vivo* fluorescence imaging of 4T1 tumor-bearing BALB/c mice treated by CuFePBA@PEGMA@AS1411/DOX and CoFePBA@PEGMA@AS1411/DOX for 30 min. As shown in Fig. 8C–E, the photon counts at the region of interest (ROI) within the 4T1 tumor-bearing nude mice treated with 0.9% saline, 0.5 mg mL^{-1} CuFePBA@PEGMA@AS1411/DOX, and 0.5% DOX were 2.640×10^4, 1.262×10^5, and 7.193×10^4, respectively. Meanwhile, the photon counts at the ROI within 4T1 tumor-bearing nude mice treated with 0.9% saline, 0.5 mg mL^{-1} CuFePBA@PEGMA@AS1411/DOX, and 0.5% DOX were 4.888×10^4, 2.116×10^5, and 9.426×10^4, respectively (Fig. 8F–H). These results show that the designed nano-DDSs accumulated in the tumor tissue, and this result can be ascribed to the AS1411-mediated recognition of DDSs and tumor cells, confirming their BC-targeting effect. Furthermore, the histological analysis of BC tumor tissues was performed in different groups (Fig. S13†). Compared with the other treatment groups, tumor cell proliferation was significantly inhibited by 1.0 mg mL^{-1} CuFePBA@PEGMA@AS1411/DOX, and tumor cells were sparsely dispersed.[57]

Subsequently, the histological examinations of crucial organs (heart, lung, spleen, liver, and kidney) from mice with different treatments were performed. Free DOX treatment caused typical histopathological changes, such as vacuolar degeneration (hepatic lesions). DOX-induced cardiotoxicity (small vacuoles in myocytes) was also observed in the DOX-treated mice (Fig. 9G). Similarly, silk sericin-based DOX-loaded NPs can mitigate DOX-induced cardiotoxicity and hepatotoxicity.[58] However, no significant histopathologic change was recorded in mice treated with CuFePBA@PEGMA@AS1411/DOX and CoFePBA@PEGMA@AS1411/DOX. Fig. S14† shows the histological examination of vital organs from healthy mice as the negative control. These results further suggest that CuFePBA@PEGMA@AS1411/DOX and CoFePBA@PEGMA@AS1411/DOX possess good biocompatibility and limited side effects.

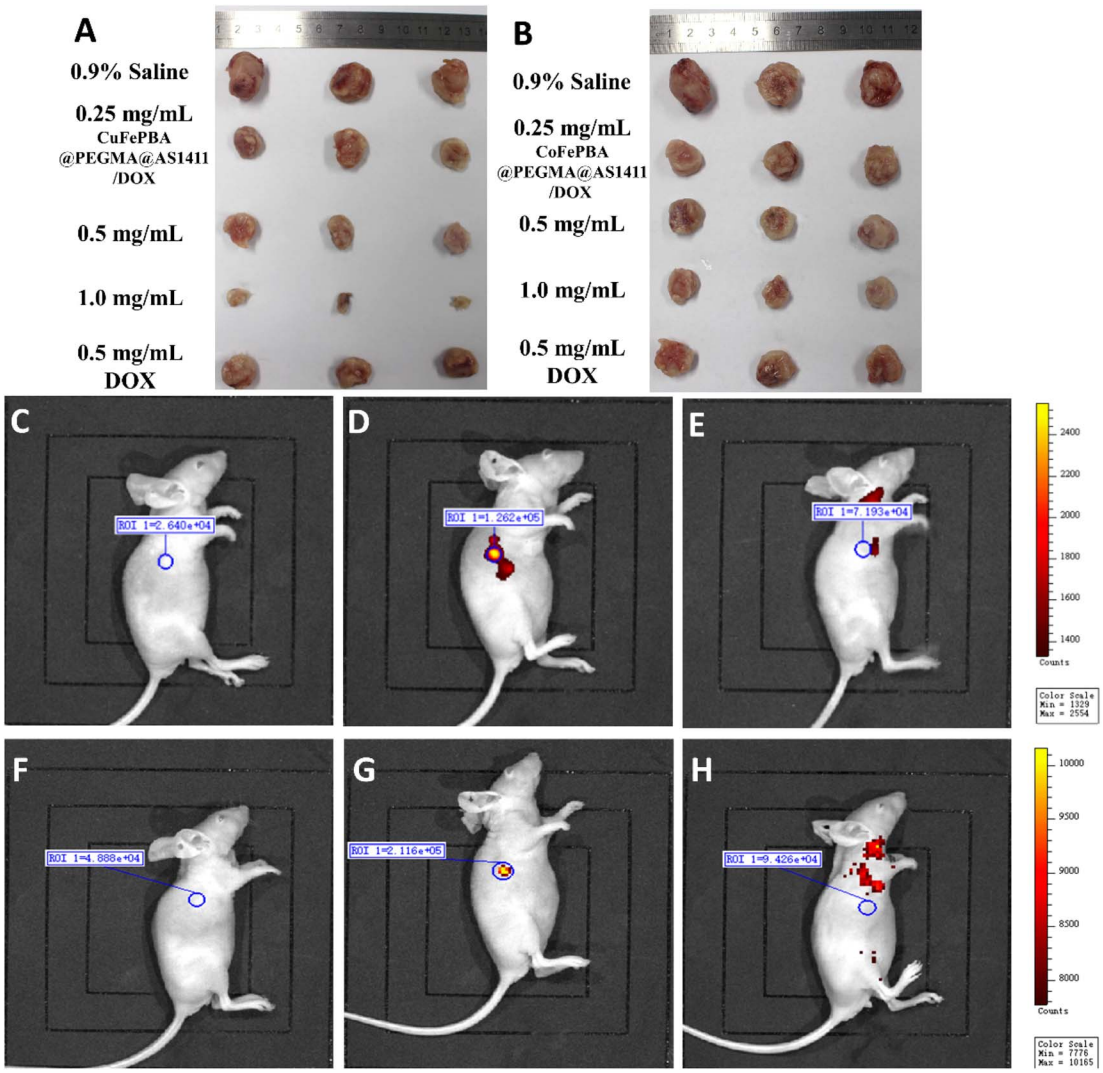

Fig. 8 *In vivo* anti-BC efficacy of CuFePBA@PEGMA@AS1411/DOX and CoFePBA@PEGMA@AS1411/DOX in 4T1 tumor-bearing mice. (A and B) Photographs of tumor tissues; (C–E) *in vivo* imaging of 4T1 tumor-bearing mice treated with 0.9% saline, 0.5 mg mL^{-1} CuFePBA@PEGMA@AS1411/DOX, and 0.5 mg mL^{-1} DOX; (F–H) *in vivo* imaging of 4T1 tumor-bearing mice treated with 0.9% saline, 0.5 mg mL^{-1} CoFePBA@PEGMA@AS1411/DOX (H) and 0.5 mg mL^{-1} DOX.

4. Discussion

BC is the most common malignancy among women.[59] It is currently treated by conventional chemotherapy, but the toxic side effects are high and therefore more optimal treatment modalities are needed.[60] Nanotechnology has developed rapidly in recent years and provides an excellent means to overcome the bottleneck of conventional therapies that cause non-specific effects on body tissues, improve the effectiveness of drug and radiation therapy, and greatly reduce adverse effects.[61–63] These materials can be used as drug carriers, imaging contrast agents, photothermal materials, photoacoustic compounds and radiation dose enhancers.[64,65]

Recently, with the increased understanding of acidic TME, it has been recognized as a new target for tumor diagnosis and treatment, which has important implications for the design of pH-responsive nanomedicines.[66] Gong *et al.* developed a pH-triggered carbon dioxide gas-generating nanoplatform based on metformin to promote T cell-mediated immune responses and enhance antitumor effects.[67] Shen *et al.* developed a robust nanoplatform made of a TME pH-responsive polymer (MEO-PEG-BPPMEMa) and a cationic lipid compound (G0–C14) that significantly enhanced the cytoplasmic uptake and subsequent intracellular escape of saponin from tumor cells, resulting in effective inhibition of tumor growth.[68] In this study, PEGMA modified CuFe-PBA and CoFe-PBA by SI-ATRP to impart good biocompatibility and excellent pH responsiveness to the nano-DDS. The designed nano-DDS showed up to 80% and 84% DOX loading efficiency, releasing about 56.0% and 75.9% DOX under acidic conditions (Fig. 3). In summary, we designed two nano-platforms with extraordinary pH responsiveness.

Aptamers are synthetically designed oligonucleotides that have been screened to bind specific targets. The process of developing aptamers is known as SELEX (systematic evolution

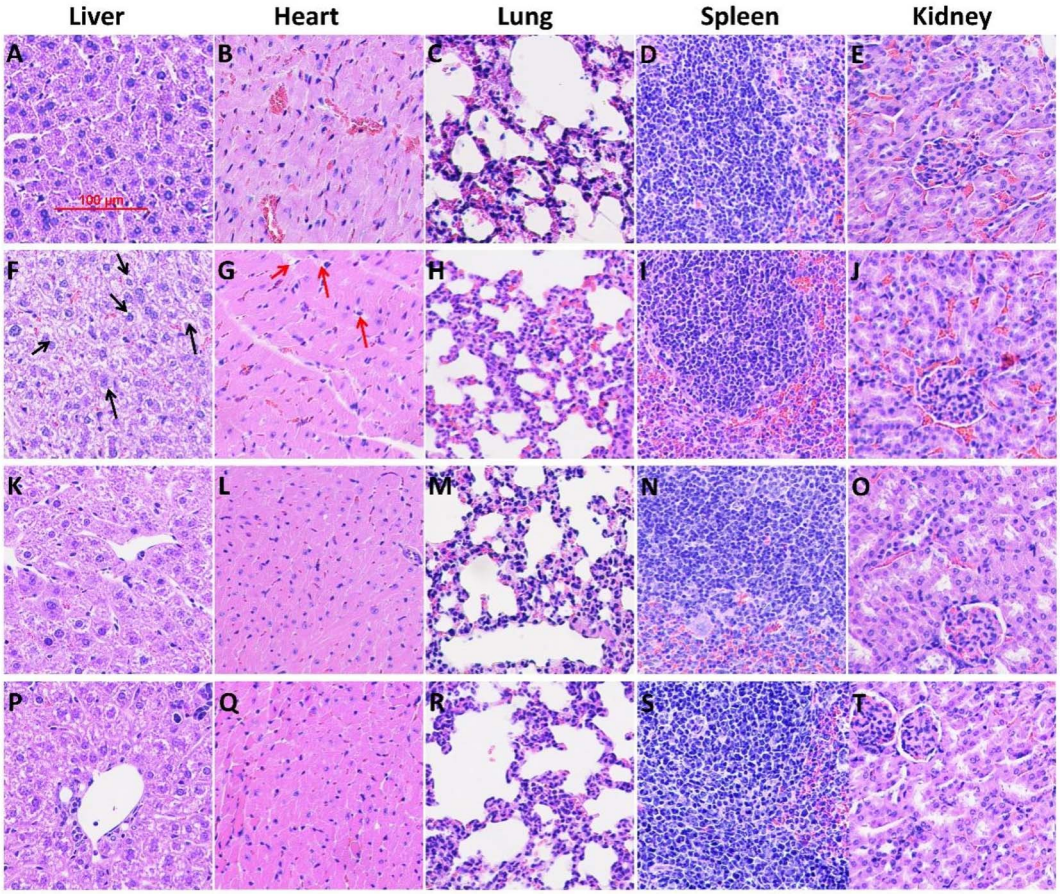

Fig. 9 Histological examination of vital organs from mice treated with (A–E) 0.9% saline, (F–J) 0.5 mg mL^{-1} DOX, (K–O) 0.5 mg mL^{-1} CuFePBA@PEGMA@AS1411/DOX, and (P–T) 0.5 mg mL^{-1} CoFePBA@PEGMA@AS1411/DOX. Black arrows indicated vacuolar degeneration, and red arrows indicated small vacuoles in myocytes. Scale bar = 100 μm.

of ligands by exponential enrichment).[69,70] Aptamers have recently been used as biomarkers to identify tumor markers and mobile tumor cells, prognostic monitoring and tumor therapy.[71] The AS1411 aptamer was shown to bind the Bcl-2 mRNA attachment protein nucleolin, which was evaluated to stimulate cytotoxicity and instability of the Bcl-2 gene in MDA-MB-231 and MCF-7 breast tumors, thereby blocking nucleolin attachment to the Bcl-2 gene and ultimately triggering the apoptotic pathway.[72] Liu *et al.* designed an AS1411–AuNSs that exhibited high durability in both serum and solution and was simply internalized by target cells at higher doses and resulted in higher anti-cytotoxic/proliferative effects compared to pure AS1411 aptamers or AuNSs.[73] In addition, *in vivo* injection of AS1411–AuNSs significantly inhibited the growth of xenograft tumors in mice without any toxic side effects.[74] Taken together, AS1411–AuNSs are suitable therapeutic candidates for clinical application in the treatment of cancer in the breast. In this study, AS1411 was immobilized in the novel PBA-DDS improving its BC targeting ability and specific uptake by BC *in vitro* and *in vivo* (Fig. 5 and 6). In addition, the novel PBA-DDS has better fluorescence, allowing the *in vivo* distribution of the drug to be clearly seen (Fig. 7). The novel PBA-DDS nanocarriers greatly reduce the side effects caused by DOX. It exhibits extraordinary *ex vivo* biocompatibility (Fig. 9) and anti-BC efficacy (Fig. 4 and 8).

Much progress has been made in the development of smart NPs for payload of anti-BC drugs, specific enrichment of tumor cells and tissues, and controlled release and efficient delivery of drugs. However, there are limitations in subcellular targeting that require continuous efforts to overcome the main obstacles, namely the design of nanocarriers based on common pathological disease states, less consideration of tumor heterogeneity, and endocytic pathways of the same nanocarriers that limit their clinical translation. We believe that through the continuous efforts of researchers, by continuously optimizing nanoparticle properties and combining different drugs, the generated novel nanoparticles can definitely bring benefits to clinical cancer patients.

5. Conclusion

In summary, novel BC-targeted nano-DDSs based on bimetallic PBAs (CuFePBA@PEGMA@AS1411/DOX and CoFePBA@PEGMA@AS1411/DOX) were developed for intracellular DOX delivery and pH-responsive drug release. PEGMA was modified against CuFe PBA and CoFe PBA *via* SI-ATRP to endow

the nano-DDSs with good biocompatibility and excellent pH response capability. The designed nano-DDSs showed as high as 80% and 84% DOX-loading efficiency, and in acidic condition, approximately 56.0% and 75.9% DOX can be released. The *in vivo* distribution results indicated that the nano-DDSs can be slowly metabolized out of the body. The *in vivo* and *in vitro* experiments showed that the novel nano-DDSs exhibited good biocompatibility, excellent tumor-targeting capability, and significant anti-BC efficacy without severe side effects. Therefore, the designed bimetallic PBA-based nano-DDSs can be secure and effective drug nano-carriers for BC chemotherapy.

Conflicts of interest

There are no conflicts to declare.

Acknowledgements

This work was supported by Medical Science and Technology Research Plan Project (SB201904005). We thank for the help of Prof. Zhihong Zhang from Zhengzhou University of Light Industry to nanoparticle synthesis.

References

1 F. Bray, J. Ferlay, I. Soerjomataram, R. L. Siegel, L. A. Torre and A. Jemal, Global cancer statistics 2018: GLOBOCAN estimates of incidence and mortality worldwide for 36 cancers in 185 countries, *Ca-Cancer J. Clin.*, 2018, **68**(6), 394–424.

2 Y. S. Yap, Y. S. Lu, K. Tamura, J. E. Lee, E. Y. Ko, Y. H. Park, A. Y. Cao, C. H. Lin, M. Toi, J. Wu and S. C. Lee, Insights Into Breast Cancer in the East vs the West: A Review, *JAMA Oncol.*, 2019, (5), 1489–1496.

3 N. Harbeck and M. Gnant, Breast cancer, *Lancet*, 2017, **389**(10074), 1134–1150.

4 X. Tang, W. S. Loc, C. Dong, G. L. Matters, P. J. Butler, M. Kester, C. Meyers, Y. Jiang and J. H. Adair, The use of nanoparticulates to treat breast cancer, *Nanomedicine*, 2017, **12**(19), 2367–2388.

5 H. Yang, W. Shen, W. Liu, L. Chen, P. Zhang, C. Xiao and X. Chen, PEGylated Poly(alpha-lipoic acid) Loaded with Doxorubicin as a pH and Reduction Dual Responsive Nanomedicine for Breast Cancer Therapy, *Biomacromolecules*, 2018, **19**(11), 4492–4503.

6 D. Wu, M. Si, H. Y. Xue and H. L. Wong, Nanomedicine applications in the treatment of breast cancer: current state of the art, *Int. J. Nanomed.*, 2017, **12**, 5879–5892.

7 H. Kulhari, D. Pooja, S. Shrivastava, M. Kuncha, V. G. M. Naidu, V. Bansal, R. Sistla and D. J. Adams, Trastuzumab-grafted PAMAM dendrimers for the selective delivery of anticancer drugs to HER2-positive breast cancer, *Sci. Rep.*, 2016, **6**, 23179.

8 Y. Wang, Y. Wang, G. Chen, Y. Li, W. Xu and S. Gong, Quantum-Dot-Based Theranostic Micelles Conjugated with an Anti-EGFR Nanobody for Triple-Negative Breast Cancer Therapy, *ACS Appl. Mater. Interfaces*, 2017, **9**(36), 30297–30305.

9 M. W. Kim, H. Y. Jeong, S. J. Kang, I. H. Jeong, M. J. Choi, Y. M. You, C. S. Im, I. H. Song, T. S. Lee, J. S. Lee, A. Lee and Y. S. Park, Anti-EGF Receptor Aptamer-Guided Co-Delivery of Anti-Cancer siRNAs and Quantum Dots for Theranostics of Triple-Negative Breast Cancer, *Theranostics*, 2019, **9**(3), 837–852.

10 A. Migotto, V. F. M. Carvalho, G. C. Salata, F. W. M. da Silva, C. Y. I. Yan, K. Ishida, L. V. Costa-Lotufo, A. A. Steiner and L. B. Lopes, Multifunctional nanoemulsions for intraductal delivery as a new platform for local treatment of breast cancer, *Drug Delivery*, 2018, **25**(1), 654–667.

11 S. Sarkar, S. Konar, P. N. Prasad, S. Rajput, B. N. P. Kumar, R. R. Rao, A. Pathak, P. B. Fisher and M. Mandal, Micellar Gold Nanoparticles as Delivery Vehicles for Dual Tyrosine Kinase Inhibitor ZD6474 for Metastatic Breast Cancer Treatment, *Langmuir*, 2017, **33**(31), 7649–7659.

12 W. Shao, A. Paul, B. Zhao, C. Lee, L. Rodes and S. Prakash, Carbon nanotube lipid drug approach for targeted delivery of a chemotherapy drug in a human breast cancer xenograft animal model, *Biomaterials*, 2013, **34**(38), 10109–10119.

13 F. Benyettou, M. Alhashimi, M. O'Connor, R. Pasricha, J. Brandel, H. Traboulsi, J. Mazher, J. C. Olsen and A. Trabolsi, Sequential Delivery of Doxorubicin and Zoledronic Acid to Breast Cancer Cells by CB[7]-Modified Iron Oxide Nanoparticles, *ACS Appl. Mater. Interfaces*, 2017, **9**(46), 40006–40016.

14 A. Pandey, N. Dhas, P. Deshmukh, C. Caro, P. Patil, M. Luisa Garcia-Martin, B. Padya, A. Nikam, T. Mehta and S. Mutalik, Heterogeneous surface architectured metal-organic frameworks for cancer therapy, imaging, and biosensing: a state-of-the-art review, *Coord. Chem. Rev.*, 2020, **409**, 213212.

15 Q. Jia, Z. Li, C. Guo, X. Huang, Y. Song, N. Zhou, M. Wang, Z. Zhang, L. He and M. Du, A gamma-cyclodextrin-based metal-organic framework embedded with graphene quantum dots and modified with PEGMA via SI-ATRP for anticancer drug delivery and therapy, *Nanoscale*, 2019, **11**(43), 20956–20967.

16 G. Zhang, X. Li, Q. Liao, Y. Liu, K. Xi, W. Huang and X. Jia, Water-dispersible PEG-curcumin/amine-functionalized covalent organic framework nanocomposites as smart carriers for in vivo drug delivery, *Nat. Commun.*, 2018, **9**(1), 2785.

17 S. K. Singh, S. Singh, J. W. Lillard Jr and R. Singh, Drug delivery approaches for breast cancer, *Int. J. Nanomed.*, 2017, **12**, 6205–6218.

18 M. X. Wu and Y. W. Yang, Metal-Organic Framework (MOF)-Based Drug/Cargo Delivery and Cancer Therapy, *Adv. Mater.*, 2017, **29**(23), e1606134.

19 K. Lu, T. Aung, N. Guo, R. Weichselbaum and W. Lin, Nanoscale Metal-Organic Frameworks for Therapeutic, Imaging, and Sensing Applications, *Adv. Mater.*, 2018, **30**(37), e1707634.

20 Z. Qin, Y. Li and N. Gu, Progress in Applications of Prussian Blue Nanoparticles in Biomedicine, *Adv. Healthcare Mater.*, 2018, **7**(20), e1800347.
21 X. Cai, W. Gao, M. Ma, M. Wu, L. Zhang, Y. Zheng, H. Chen and J. Shi, A Prussian Blue-Based Core-Shell Hollow-Structured Mesoporous Nanoparticle as a Smart Theranostic Agent with Ultrahigh pH-Responsive Longitudinal Relaxivity, *Adv. Mater.*, 2015, **27**(41), 6382–6389.
22 J. Li, F. Zhang, Z. Hu, W. Song, G. Li, G. Liang, J. Zhou, K. Li, Y. Cao, Z. Luo and K. Cai, Drug "Pent-Up" in Hollow Magnetic Prussian Blue Nanoparticles for NIR-Induced Chemo-Photothermal Tumor Therapy with Trimodal Imaging, *Adv. Healthcare Mater.*, 2017, **6**(14), e1700005.
23 M. Gautam, K. Poudel, C. S. Yong and J. O. Kim, Prussian blue nanoparticles: synthesis, surface modification, and application in cancer treatment, *Int. J. Pharm.*, 2018, **549**(1–2), 31–49.
24 W. Tian, Y. Su, Y. Tian, S. Wang, X. Su, Y. Liu, Y. Zhang, Y. Tang, Q. Ni, W. Liu, M. Dang, C. Wang, J. Zhang, Z. Teng and G. Lu, Periodic Mesoporous Organosilica Coated Prussian Blue for MR/PA Dual-Modal Imaging-Guided Photothermal-Chemotherapy of Triple Negative Breast Cancer, *Adv. Sci.*, 2017, **4**(3), 1600356.
25 M. Gautam, K. Poudel, C. S. Yong and J. O. Kim, Prussian blue nanoparticles: synthesis, surface modification, and application in cancer treatment, *Int. J. Pharm.*, 2018, **549**(1–2), 31–49.
26 Q. Jia, L. Zhenzhen, C. Guo, X. Huang, M. Kang, Y. Song, L. He, N. Zhou, M. Wang, Z. Zhang, G. Fu and M. Du, PEGMA-modified bimetallic NiCo Prussian blue analogue doped with Tb(III) ions: efficiently pH-responsive and controlled release system for anticancer drug, *Chem. Eng. J.*, 2020, **389**, 124468.
27 Y. Liu, L. Qiao, S. Zhang, G. Wan, B. Chen, P. Zhou, N. Zhang and Y. Wang, Dual pH-responsive multifunctional nanoparticles for targeted treatment of breast cancer by combining immunotherapy and chemotherapy, *Acta Biomater.*, 2018, **66**, 310–324.
28 Q. Jia, F. Su, Z. Li, X. Huang, L. He, M. Wang, Z. Zhang, S. Fang and N. Zhou, Tunable Hollow Bimetallic MnFe Prussian Blue Analogue as the Targeted pH-Responsive Delivery System for Anticancer Drugs, *ACS Appl. Bio Mater.*, 2019, **2**(5), 2143–2154.
29 J. Wang, S. S. A. Zaidi, A. Hasnain, J. T. Guo, X. K. Ren, S. H. Xia, W. C. Zhang and Y. K. Feng, Multitargeting Peptide-Functionalized Star-Shaped Copolymers with Comblike Structure and a POSS-Core To Effectively Transfect Endothelial Cells, *ACS Biomater. Sci. Eng.*, 2018, **4**(6), 2155–2168.
30 S. V. Lale, R. G. Aswathy, A. Aravind, D. S. Kumar and V. Koul, AS1411 Aptamer and Folic Acid Functionalized pH-Responsive ATRP Fabricated pPEGMA-PCL-pPEGMA Polymeric Nanoparticles for Targeted Drug Delivery in Cancer Therapy, *Biomacromolecules*, 2014, **15**(5), 1737–1752.
31 C. Huang, K. G. Neoh and E. T. Kang, Combined ATRP and 'Click' Chemistry for Designing Stable Tumor-Targeting Superparamagnetic Iron Oxide Nanoparticles, *Langmuir*, 2012, **28**(1), 563–571.
32 K. Matyjaszewski, Advanced Materials by Atom Transfer Radical Polymerization, *Adv. Mater.*, 2018, **30**(23), e1706441.
33 J. O. Zoppe, N. C. Ataman, P. Mocny, J. Wang, J. Moraes and H. A. Klok, Surface-Initiated Controlled Radical Polymerization: State-of-the-Art, Opportunities, and Challenges in Surface and Interface Engineering with Polymer Brushes, *Chem. Rev.*, 2017, **117**(3), 1105–1318.
34 M. Kanamala, W. R. Wilson, M. Yang, B. D. Palmer and Z. Wu, Mechanisms and biomaterials in pH-responsive tumour targeted drug delivery: a review, *Biomaterials*, 2016, **85**, 152–167.
35 L. K. Parrott and E. Erasmus, Metal Hexacyanometallate Nanoparticles: Spectroscopic Investigation on the Influence of Oxidation State of Metals on Catalytic Activity, *Catal. Lett.*, 2018, **148**(7), 2008–2018.
36 Z. Chen, S. Chen, Y. Li, X. Si, J. Huang, S. Massey and G. Chen, A recyclable and highly active Co_3O_4 nanoparticles/titanate nanowire catalyst for organic dyes degradation with peroxymonosulfate, *Mater. Res. Bull.*, 2014, **57**, 170–176.
37 S. Rella, E. Mazzotta, A. Caroli, M. De Luca, C. Bucci and C. Malitesta, Investigation of polydopamine coatings by X-ray photoelectron spectroscopy as an effective tool for improving biomolecule conjugation, *Appl. Surf. Sci.*, 2018, **447**, 31–39.
38 S. Gerber and E. Erasmus, Electronic effects of metal hexacyanoferrates: an XPS and FTIR study, *Mater. Chem. Phys.*, 2018, **203**, 73–81.
39 G. Yang, Y. Shen, M. Wang, H. Chen, B. Liu and S. Dong, Copper hexacyanoferrate multilayer films on glassy carbon electrode modified with 4-aminobenzoic acid in aqueous solution, *Talanta*, 2006, **68**(3), 741–747.
40 W. Bian, G. Zhao and J. Nishii, The Effect of Heating Temperature in Ultraviolet Irradiation Process on Properties of $YBa_2Cu_3O_{7-x}$ Superconducting Films Processed From Photosensitive Solution, *IEEE Trans. Appl. Supercond.*, 2019, **30**(1), 1–5.
41 A. Lisowska-Oleksiak, M. Wilamowska and V. Jasulaitiené, Organic–inorganic composites consisted of poly(3,4-ethylenedioxythiophene) and Prussian blue analogues, *Electrochim. Acta*, 2011, **56**(10), 3626–3632.
42 M. C. Biesinger, L. W. M. Lau, A. R. Gerson and R. S. C. Smart, Resolving surface chemical states in XPS analysis of first row transition metals, oxides and hydroxides: Sc, Ti, V, Cu and Zn, *Appl. Surf. Sci.*, 2010, **257**, 887–898.
43 M. A. Amer, A. Matsuda, G. Kawamura, R. El-Shater, T. Meaz and F. Fakhry, Characterization and structural and magnetic studies of as-synthesized $Fe^{2+}Cr_xFe_{(2-x)}O_4$ nanoparticles, *J. Magn. Magn. Mater.*, 2017, **439**, 373–383.
44 Z. Zhang, X. Wang, K. C. Tam and G. Sebe, A Comparative Study on Grafting Polymers from Cellulose Nanocrystals via Surface-Initiated Atom Transfer Radical Polymerization (ATRP) and Activator Regenerated by Electron Transfer ATRP, *Carbohydr. Polym.*, 2019, **205**, 322–329.

45 J. Jaafar, N. Kamarudin, H. Setiabudi, S. Timmiati and T. Peng, Mesoporous Silica Nanoparticles and Waste Derived-Siliceous Materials for Doxorubicin Adsorption and Release, *Mater. Today: Proc.*, 2019, **19**, 1420–1425.

46 X. Yang, T. Yong-Bing, X. Huang, H. Xue, W. Kang, W. Li, T. Ng and C. Lee, Lithium ion battery application of porous composite oxide microcubes prepared via metal-organic frameworks, *J. Power Sources*, 2015, **284**, 109–114.

47 X. Jia, X. Zhao, K. Tian, T. Zhou, J. Li, R. Zhang and P. Liu, Fluorescent Copolymer-Based Prodrug for pH-Triggered Intracellular Release of DOX, *Biomacromolecules*, 2015, **16**(11), 3624–3631.

48 I. Abanades Lazaro, S. Haddad, S. Sacca, C. Orellana-Tavra, D. Fairen-Jimenez and R. S. Forgan, Selective Surface PEGylation of UiO-66 Nanoparticles for Enhanced Stability, Cell Uptake, and pH-Responsive Drug Delivery, *Chem*, 2017, **2**(4), 561–578.

49 W. Chen, K. Zeng, H. Liu, J. Ouyang, L. Wang, Y. Liu, H. Wang, L. Deng and Y.-N. Liu, Cell Membrane Camouflaged Hollow Prussian Blue Nanoparticles for Synergistic Photothermal-/Chemotherapy of Cancer, *Adv. Funct. Mater.*, 2017, **27**(11), e1605795.

50 S. M. Taghdisi, N. M. Danesh, M. Ramezani, R. Yazdian-Robati and K. Abnous, A Novel AS1411 Aptamer-Based Three-Way Junction Pocket DNA Nanostructure Loaded with Doxorubicin for Targeting Cancer Cells in Vitro and in Vivo, *Mol. Pharm.*, 2018, **15**(5), 1972–1978.

51 P. J. Bates, E. M. Reyes-Reyes, M. T. Malik, E. M. Murphy, M. G. O'Toole and J. O. Trent, G-quadruplex oligonucleotide AS1411 as a cancer-targeting agent: uses and mechanisms, *Biochim. Biophys. Acta, Gen. Subj.*, 2017, **1861**(5 Pt B), 1414–1428.

52 Y. Wang, X. Chen, B. Tian, J. Liu, L. Yang, L. Zeng, T. Chen, A. Hong and X. Wang, Nucleolin-targeted Extracellular Vesicles as a Versatile Platform for Biologics Delivery to Breast Cancer, *Theranostics*, 2017, **7**(5), 1360–1372.

53 Z. X. Liao, E. Y. Chuang, C. C. Lin, Y. C. Ho, K. J. Lin, P. Y. Cheng, K. J. Chen, H. J. Wei and H. W. Sung, An AS1411 aptamer-conjugated liposomal system containing a bubble-generating agent for tumor-specific chemotherapy that overcomes multidrug resistance, *J. Controlled Release*, 2015, **208**, 42–51.

54 D. H. Dam, R. C. Lee and T. W. Odom, Improved in vitro efficacy of gold nanoconstructs by increased loading of G-quadruplex aptamer, *Nano Lett.*, 2014, **14**(5), 2843–2848.

55 Q. Zhu, H. Qi, Z. Long, S. Liu, Z. Huang, J. Zhang, C. Wang and L. Dong, Extracellular control of intracellular drug release for enhanced safety of anti-cancer chemotherapy, *Sci. Rep.*, 2016, **6**, 28596.

56 C. Peng, J. Xu, M. Yu, X. Ning, Y. Huang, B. Du, E. Hernandez, P. Kapur, J. T. Hsieh and J. Zheng, Tuning the In Vivo Transport of Anticancer Drugs Using Renal-Clearable Gold Nanoparticles, *Angew. Chem., Int. Ed.*, 2019, **58**(25), 8479–8483.

57 P. Wu, Y. Sun, W. Dong, H. Zhou, S. Guo, L. Zhang, X. Wang, M. Wan and Y. Zong, Enhanced anti-tumor efficacy of hyaluronic acid modified nanocomposites combined with sonochemotherapy against subcutaneous and metastatic breast tumors, *Nanoscale*, 2019, **11**(24), 11470–11483.

58 D. Hu, T. Li, Z. Xu, D. Liu, M. Yang and L. Zhu, Self-stabilized silk sericin-based nanoparticles: in vivo biocompatibility and reduced doxorubicin-induced toxicity, *Acta Biomater.*, 2018, **74**, 385–396.

59 J. Ferlay, M. Colombet, I. Soerjomataram, D. M. Parkin, M. Piñeros, A. Znaor and F. Bray, Cancer statistics for the year 2020: an overview, *Int. J. Cancer*, 2021, **149**, 778–789.

60 P. Gupta, Y. R. Neupane, S. Parvez and K. Kohli, Recent advances in targeted nanotherapeutic approaches for breast cancer management, *Nanomedicine*, 2021, **16**, 2605–2631.

61 C. Huang, Z. Liu, M. Chen, L. Du, C. Liu, S. Wang, Y. Zheng and W. Liu, *J. Nanobiotechnol.*, 2021, **19**, 457.

62 Y. Li, Z. Liu, W. Zeng, Z. Wang, C. Liu, N. Zeng, K. Zhong, D. Jiang and Y. Wu, Tumor-derived biomimetic nanozyme with immune evasion ability for synergistically enhanced low dose radiotherapy, *Front. Oncol.*, 2021, **11**, 738567.

63 N. Zeng, X. Chen and Z. Liu, Natural Products and Nanotechnology Against Coronavirus Disease 2019, *Front. Chem.*, 2022, **10**, 819969.

64 P. Kielbik, J. Kaszewski, S. Dabrowski, R. Faundez, B. S. Witkowski, L. Wachnicki, Y. Zhydachevskyy, R. Sapierzynski, Z. Gajewski, M. Godlewski and M. M. Godlewski, Transfer of orally administered ZnO:Eu nanoparticles through the blood-testis barrier: the effect on kinetic sperm parameters and apoptosis in mice testes, *Nanotechnology*, 2019, **30**, 455101.

65 J. B. Vines, J. H. Yoon, N. E. Ryu, D. J. Lim and H. Park, Gold Nanoparticles for Photothermal Cancer Therapy, *Front. Chem.*, 2019, **7**, 167.

66 J. Li, Y. Wang, C. Xu, Q. Yu, X. Wang, H. Xie, L. Tian, Y. Qiu, R. Guo, Z. Lu, M. Li and Q. He, Rapid pH-responsive self-disintegrating nanoassemblies balance tumor accumulation and penetration for enhanced anti-breast cancer therapy, *Acta Biomater.*, 2021, **134**, 546–558.

67 C. Gong, X. Yu, W. Zhang, L. Han, R. Wang, Y. Wang, S. Gao and Y. Yuan, Regulating the immunosuppressive tumor microenvironment to enhance breast cancer immunotherapy using pH-responsive hybrid membrane-coated nanoparticles, *J. Nanobiotechnol.*, 2021, **19**, 58.

68 Q. Shen, L. Xu, R. Li, G. Wu, S. Li, P. E. Saw, Y. Zhou and X. Xu, A tumor microenvironment (TME)-responsive nanoplatform for systemic saporin delivery and effective breast cancer therapy, *Chem. Commun.*, 2021, **57**, 2563–2566.

69 H. Kaur, Recent developments in cell-SELEX technology for aptamer selection, *Biochim. Biophys. Acta, Gen. Subj.*, 2018, **1862**, 2323–2329.

70 T. Wang, C. Chen, L. M. Larcher, R. A. Barrero and R. N. Veedu, Three decades of nucleic acid aptamer technologies: lessons learned, progress and opportunities on aptamer development, *Biotechnol. Adv.*, 2019, **37**, 28–50.

71 M. Gijs, G. Penner, G. B. Blackler, N. R. E. N. Impens, S. Baatout, A. Luxen and A. M. Aerts, Improved Aptamers for the Diagnosis and Potential Treatment of HER2-Positive Cancer, *Pharmaceuticals*, 2016, **9**, 29.

72 L. E. Ibarra, S. Camorani, L. Agnello, E. Pedone, L. Pirone, C. A. Chesta, R. E. Palacios, M. Fedele and L. Cerchia, Selective Photo-Assisted Eradication of Triple-Negative Breast Cancer Cells through Aptamer Decoration of Doped Conjugated Polymer Nanoparticles, *Pharmaceutics*, 2022, **14**, 626.

73 Y. Liu, M. Ding, K. Guo, Z. Wang, C. Zhang and Q. T. H. Shubhra, Systemic Co-delivery of drugs by a pH- and photosensitive smart nanocarrier to treat cancer by chemo-photothermal-starvation combination therapy, *Smart Materials in Medicine*, 2022, **3**, 390–403.

74 T. Gholikhani, S. Kumar, H. Valizadeh, S. Mahdinloo, K. Adibkia, P. Zakeri-Milani, M. Barzegar-Jalali and B. Jimenez, Advances in Aptamers-Based Applications in Breast Cancer: Drug Delivery, Therapeutics, and Diagnostics, *Int. J. Mol. Sci.*, 2022, **23**, 14475.